

Article

Motion Error Estimation and Compensation of Airborne Array Flexible SAR Based on Multi-Channel Interferometric Phase

Ling Yang ^{1,2}, Fubo Zhang ^{1,*}, Yihong Sun ³, Longyong Chen ¹, Zhenhua Li ^{1,2} and Dawei Wang ^{1,2}

¹ National Key Laboratory of Microwave Imaging Technology, Aerospace Information Research Institute, Chinese Academy of Sciences, Beijing 100190, China

² School of Electronic, Electrical and Communication Engineering, University of Chinese Academy of Sciences, Beijing 100094, China

³ School of Instrumentation and Optoelectronic Engineering, Beihang University, Beijing 100094, China

* Correspondence: zhangfb@aircas.ac.cn

Abstract: Airborne array synthetic aperture radar (SAR) has made a significant breakthrough in the three-dimensional resolution of traditional SAR. In the airborne array SAR 3D imaging technology, the baseline length is the main factor restricting the resolution. Airborne array flexible SAR can increase the baseline length to improve the resolution and interference performance by mounting antennae on the wing. The existing research lacks results obtained using flexible actual data processing and specific motion compensation methods. Thus, this paper proposes a motion error estimation and compensation method for an airborne array flexible SAR based on a multi-channel interferometric phase. Firstly, a flexible channel motion compensation model is established based on the multi-channel interference phase of airborne array flexible SAR. Then, based on the rigid multi-channel data, combined with the ground control points, the least square method, and the global optimal search algorithm, the accurate rigid baseline length and the central incidence angle are obtained. Finally, according to the multi-channel interference phase inversion of the flexible motion error and combined with the motion compensation model, the flexible data are compensated in the time domain. The actual results indicate that, compared with traditional motion compensation methods, our method can obtain accurate flexible compensation data. This study improves the interference performance of multi-channel data of airborne array flexible SAR and lays a solid foundation for the high-precision 3D reconstruction of airborne array flexible SAR.



Citation: Yang, L.; Zhang, F.; Sun, Y.; Chen, L.; Li, Z.; Wang, D. Motion Error Estimation and Compensation of Airborne Array Flexible SAR Based on Multi-Channel Interferometric Phase. *Remote Sens.* **2023**, *15*, 680. <https://doi.org/10.3390/rs15030680>

Academic Editor: Lorenzo Capineri

Received: 3 December 2022

Revised: 18 January 2023

Accepted: 18 January 2023

Published: 23 January 2023



Copyright: © 2023 by the authors. Licensee MDPI, Basel, Switzerland. This article is an open access article distributed under the terms and conditions of the Creative Commons Attribution (CC BY) license (<https://creativecommons.org/licenses/by/4.0/>).

1. Introduction

Airborne array synthetic aperture radar (SAR) has a pivotal position in three-dimensional (3D) applications of SAR because it can obtain 3D scene information in a single pass. Airborne array SAR has strong application prospects in urban surveying and mapping [1], topographic survey [2], rescue and disaster relief [3], meteorological monitoring [4], resource exploration [5], and other aspects [6,7].

Many indicators of airborne array SAR, such as positioning accuracy, Digital Elevation Model (DEM) accuracy, 3D resolution, etc., are closely related to the baseline length. However, the existing airborne systems are limited by the width of the fuselage abdomen, and the baseline length is often insufficient. Conducting high-precision mapping based on the existing systems is the mainstream research direction [8–10]. Some scholars proposed extending the baseline, mounting the antenna on the wing or extending the device with an antenna to develop a system with high positioning accuracy, high DEM accuracy, and high 3D resolution [11]. Since the antenna is mounted on a device with an unfixed wing, not a rigid platform on the belly, it is called an array flexible SAR system.

The construction of array flexible SAR systems can be traced back to the Shuttle Radar Topography Mission (SRTM) launched by the United States, which aims to obtain global elevation information [12]. This system has a rigid baseline of 20 m and a scalable flexible baseline of 60 m. However, the existing DEM open-source results on SRTM are all obtained by processing with a rigid baseline of 20 m, and there are no relevant processing results on flexible data [13]. Another actual system is the European unmanned aerial vehicle Airborne Radar for Three-dimensional Imaging and Nadir Observation (ARTINO), which aims to quickly obtain DEM information of observation scenes to overcome the disadvantage of a long revisit period on satellite [14]. It attaches an antenna to the middle part of the wing on one side, and carries a rigid antenna with multiple transmitters and receivers on the belly to complete the observation. To date, there has been no report on its wing antenna results. The literature does not recommend using a flexible baseline [15].

The Aerospace Information Research Institute, Chinese Academy of Sciences (AIRCAS) conducted an equivalent experiment of array flexible SAR in Chengdu, Sichuan Province in 2021. The system consisted of two receiving and transmitting antennas and three receiving antennas. The two receiving antennas placed outside were controlled by motors to simulate flexible jitters and obtained the first flight data of an airborne array flexible SAR in China. Rigid antenna nodes were used for transmitting signals. Meanwhile, the distributed Position and Orientation System (POS) was carried out to measure the tracks of rigid nodes and flexible nodes, which were mounted on the center of the rigid structure and two flexible antennas, respectively. This flight test laid a solid foundation for research on airborne array flexible SAR.

In terms of array SAR motion error estimation and compensation, existing studies mainly focus on the estimation and compensation of rigid, time-varying, baseline motion errors [16,17]. The main research directions are radar data compensation and navigation data correction. For radar data compensation, D. You et al. [18] proposed a baseline estimation and compensation method based on sub-aperture. H. Wang et al. [19] provided a modeling and estimation method for residual motion errors. A residual baseline estimation method based on time-domain back projection and multi-order technology was proposed by N. Cao et al. [20]. For navigation data correction, Y. Liu et al. [21] developed a navigation data correction method based on Kalman estimation. Due to its lack of array flexible SAR systems, this method was less studied. G. Franceschetti et al. [22] analyzed the causes and influencing factors regarding the flexible baseline of SRTM systems. B. Wang et al. [23] presented a method to correct POS data by combining rigid interferogram inversion with a flexible baseline length. B. Gu et al. [24] proposed a method to measure the flexible baseline of distributed POS. Moreover, Y. Sun et al. [25] mainly investigated the navigation transfer alignment algorithm to obtain POS data with a higher precision.

Due to the unique attributes of the array flexible SAR systems, the existing methods cannot be directly applied and should be improved accordingly. The existing POS processing technology is in a highly developed stage. To solve the key problem of the real-time, high-precision measurement of multi-point motion parameters, the Beihang team proposed a transfer alignment method based on the federal filter [26]. Meanwhile, as it is difficult for multi-sensors to obtain information accurately, which leads to data fusion errors, a multi-sensor time-synchronization error modeling and compensation method is proposed [27]. An accelerometer-based deformation measurement method and an innovative distributed filter are proposed for flexible deformation measurement [28]. The processing accuracy of interferometric SAR needs to reach the millimeter level, so the development of high-precision POS by Y. Sun et al. [25] cannot meet the requirements. In the imaging process of array flexible SAR systems, the antenna phase center is also time-varying, and many existing imaging methods focus on the fixed-phase center, so it is necessary to study the matching imaging method. The motion error estimation and compensation methods should be investigated for the special problems that occur in the actual array flexible SAR system.

To solve the above problems, this paper proposes a flexible channel motion error estimation and compensation method based on multi-channel interferograms of airborne

array flexible SAR. Firstly, a flexible channel motion compensation model based on the multi-channel interference phase of airborne array flexible SAR is established. Then, based on the rigid multi-channel data and combined with the ground control points, the accurate rigid baseline length and the central incidence angle are obtained through the least square method and the global optimal search algorithm. Finally, according to the rigid channel interferogram inversion residual error and combined with the motion compensation model, the flexible data are compensated in the time domain. The main innovation of this paper is proposing an improved algorithm to address the poor coherence of airborne array flexible SAR data. This can not only improve the interference performance of multi-channel data, but can also improve the coherence of multi-channel data, laying a solid foundation for the high-precision mapping of array flexible SAR.

The rest of this paper is as follows. Section 2 presents the motion compensation model, imaging model, and the corresponding parameter calculation theory of airborne array flexible SAR. Section 3 introduces the method proposed in this paper. In Sections 4 and 5, the flight data of the airborne array flexible SAR system of the AIRCAS are exploited to verify the effectiveness of the proposed method. Finally, Sections 6 and 7 present the results, discussion and conclusion, respectively.

2. Theory

In this section, the imaging model and motion compensation theory for an airborne array flexible SAR are presented first. Then, the least square method is combined with the global optimal search algorithm to obtain an accurate perspective. Finally, the calculation and compensation method of determining airborne array flexible SAR motion errors is proved.

2.1. 3D Imaging Model and Motion Compensation Theory of Airborne Array Flexible SAR

The airborne array flexible SAR has a third-dimension resolution (i.e., height resolution). This is obtained by adding multiple antennas across the course to form a height-oriented synthetic aperture. The main factor limiting the elevation resolution of airborne array tomographic SAR is the length of the baseline across the course. Thus, some scholars proposed mounting antennas on the wing to form a long baseline, thus breaking the limit. The flexible mounting diagram of airborne array tomographic SAR is illustrated in Figure 1.

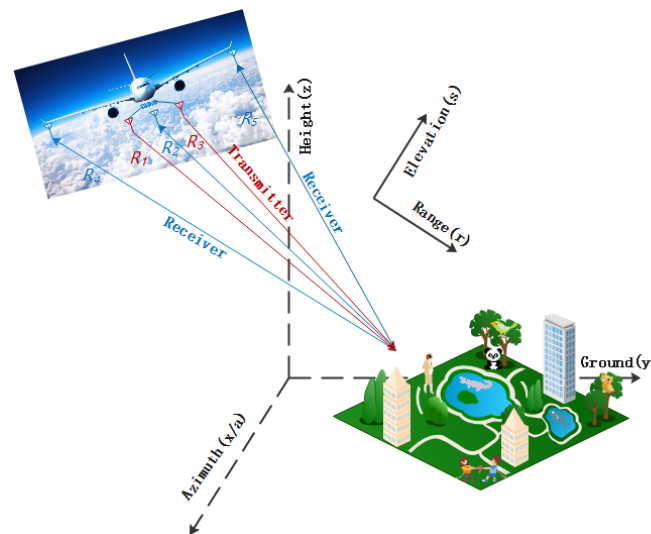


Figure 1. The schematic diagram of flexible mounting of airborne array flexible SAR.

Two different coordinate systems, namely, the geodetic coordinate system and radar coordinate system, are presented in Figure 1. The geodetic coordinate system involves the direction of azimuth, ground distance, and height, while the radar coordinate system involves the direction of azimuth, slant distance, and elevation, which are perpendicular to

each other. The two coordinate systems follow the principle of the right-hand coordinate system. The transmitting antenna is located on the belly of the fuselage, and the receiving antenna is mounted on the belly of the fuselage and the wing. Based on this, stable calibration results were obtained by forming a rigid baseline with three antennae attached to the fuselage abdomen, and long baseline results were obtained by forming a flexible baseline with two antennae attached to the wing.

The transmitted signal [29] is a linear frequency modulation (LFM) signal, and the expression is shown in Equation (1).

$$s(t) = \text{rect}\left(\frac{t}{T_p}\right) \exp\{j2\pi f_0 t + j\pi K_r t^2\} \quad (1)$$

where t , T_p , and f_0 denote the distance and speed, the transmit pulse width, and the center frequency, respectively; K_r represents the linear tuning frequency. The signal received after a fixed delay is represented in Equation (2).

$$s_{r1}(t, \tau) = \sum_i \left\{ \sigma_i \cdot \text{rect}\left(\frac{t - R_\tau/c}{T_p}\right) \exp\left\{-j4\pi f_0 \frac{R_\tau}{c}\right\} \exp\left\{-j\pi K_r \left(\tau - \frac{2R_\tau}{c}\right)^2\right\} \right\} \quad (2)$$

where $R_\tau = R_1 - R_4$, R_1 and R_4 are, respectively, the distance from the rigid node to the target and the distance from the target to the flexible node. After filtering with a 3D matched filter, the signal through 3D Fourier transform [30] is expressed in Equation (3).

$$s_{r2}(x, y, z) = \sum_i \sigma_i \sin c\left[\frac{B_{x_i}(x - x_i)}{2\pi}\right] \sin c\left[\frac{B_{y_i}(y - y_i)}{2\pi}\right] \sin c\left[\frac{B_{z_i}(z - z_i)}{2\pi}\right] \quad (3)$$

where B_{x_i} , B_{y_i} , and B_{z_i} are the bandwidth of the target azimuth beam support domain, the target cross-heading beam support domain, the target elevation beam support domain, respectively.

The multi-channel interference phase can be obtained from the processed signal after multi-channel registration [31]. The details are shown in Equation (4).

$$\Delta\phi = -\frac{4\pi}{\lambda}(R_1 - R_2) \quad (4)$$

where $\Delta\phi$ is the interference phase of the rigid channel and the flexible channel.

The complex image $s_1(m, n)$ and $s_2(m, n)$ between two channels can calculate the coherence coefficient of the complex image pair, and the expression is shown in Equation (5).

$$r = \frac{\left| \sum_{m=1}^M \sum_{n=1}^N s_1(m, n) \cdot s_2^*(m, n) \right|}{\sqrt{\sum_{m=1}^M \sum_{n=1}^N |s_1(m, n)|^2 \sum_{m=1}^M \sum_{n=1}^N |s_2(m, n)|^2}} \quad (5)$$

2.2. Central Incidence Angle for Airborne Array Flexible SAR

In this system, the measurement geometry of three-channel calibration for airborne array SAR is shown in Figure 2. In this figure, A_1 and A_3 are transmitting antennas, A_1 , A_2 , and A_3 are receiving antennas, and the slant distances to the point targets are R_1 , R_2 , and R_3 , respectively. As the three antenna connections are rigid connections, the baseline inclination is α_1 , the corresponding central incidence angle is θ , and the carrier height is H .

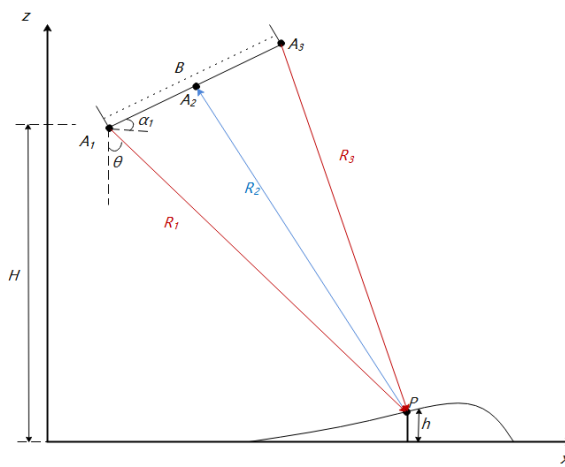


Figure 2. The measurement geometry of three channel calibration of airborne array flexible SAR.

The expression of baseline length and central incidence angle could be obtained by approximating Equation (1), as shown in Equation (6).

$$\begin{aligned}
 \Delta\varphi &= \varphi_1 - \varphi_2 \\
 &= -\frac{4\pi}{\lambda}(R_1 - R_2) - \frac{4\pi}{\lambda}(R_2 - R_3) \\
 &= -\frac{4\pi}{\lambda}(R_1 - R_3) \\
 &\approx -\frac{4\pi}{\lambda}B \sin(\theta - \alpha) \\
 &= -\frac{4\pi}{\lambda}(B_x \sin \alpha - B_y \cos \alpha)
 \end{aligned} \tag{6}$$

where $B_x = B \sin \theta$ is the horizontal component of the baseline and $B_y = B \cos \theta$ is the vertical component of the baseline. The optimization function is constructed based on the least square method. The baseline length, dip angle, and initial phase are calculated through the ground calibration points. The optimization function [23] is shown in Equation (7).

$$F(B, \alpha) = \min \left(\Delta\varphi + \frac{4\pi}{\lambda} B \sin(\theta - \alpha) \right) \tag{7}$$

Then, Equation (7) is combined with the target height function, as shown in Equation (8).

$$h = H - R_1 \cos \theta \tag{8}$$

Next, combined with the global optimal search algorithm, the length and inclination of the rigid baseline can be calculated by constructing the minimization function, as shown in Equation (9).

$$F(B, \alpha) = \min \left(H - h - R_1 \cos \left(\arcsin \left(\frac{B}{4\pi} \cdot \frac{\Delta\varphi}{\lambda} \right) + \alpha \right) \right) \tag{9}$$

According to the results of the above formula, the central incidence angle can be obtained. The specific calculation is presented in Equation (10).

$$\theta = \arcsin \left(\frac{B}{4\pi} \cdot \frac{\Delta\varphi}{\lambda} \right) + \alpha \tag{10}$$

Through the above steps, the central incidence angle of the scene can be obtained, which provides a basis for the subsequent airborne array flexible SAR motion error conversion.

2.3. Motion Error Calculation of Airborne Array Flexible SAR

Under the system shown in Figure 1, the geometric measurement of the flexible baseline is shown in Figure 3. In this figure, A_4 and A_5 are flexible antennas; the blue arrow indicates the position of the POS system measurement antenna, and the corresponding slant distance is R_4 and R_5 . The sum in red is the measurement error ΔR_4 and ΔR_5 ; the corresponding antenna position is A'_4 and A'_5 , respectively.

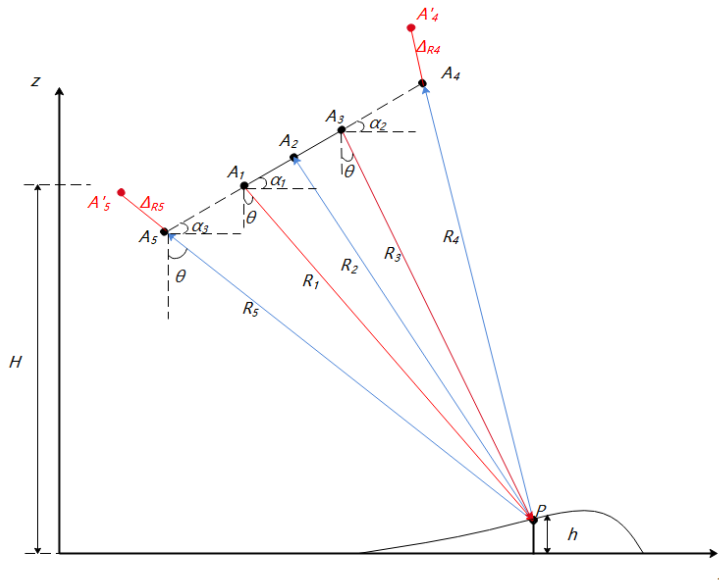


Figure 3. The schematic diagram of geometric measurement of the flexible baseline.

The above figure shows that, for the flexible antenna A_5 , the measured slant distance is R_5 , the real moving point is A_5 , and the real distance is presented in Equation (11).

$$R'_5 = R_5 + \Delta R_5 \quad (11)$$

The issues in obtaining the offset urgently need to be addressed. The interference between the flexible antenna and the rigid antenna can be expressed in Equation (12).

$$\varphi_5 = -\frac{4\pi}{\lambda}(R_1 - R'_5) = -\frac{4\pi}{\lambda}(R_1 - R_5 + \Delta R_5) \quad (12)$$

According to Section 2.2, the interference phase changed for $\lambda/2$ cycles from $[-\pi, \pi]$. By obtaining the offset $\Delta\varphi$ from the interference phase diagram and calculating the proportion of $\Delta\varphi$ in the total cycle φ , the offset ΔR is determined, as shown in Equation (13).

$$\Delta R = \frac{\Delta\varphi}{\varphi} \cdot \frac{\lambda}{2} \quad (13)$$

The flexible change can be obtained by ΔR . Meanwhile, the calibration result can be obtained by Section 2.3 to obtain the lower viewing angle θ . The projection of the error in the ground distance and elevation direction is shown in Equations (14) and (15), respectively.

$$\Delta R_z = \Delta R \cos \theta \quad (14)$$

$$\Delta R_y = -\Delta R \sin \theta \quad (15)$$

The above error results are added to the data before motion compensation to obtain accurate compensation data, and then two-dimensional (2D) imaging is conducted to obtain better 2D images and interferograms through multiple iterations.

Based on the above theoretical analysis, the method proposed in this paper is introduced in the following.

3. Method

This paper proposes a flexible channel motion compensation method based on multi-channel interferograms of airborne array flexible SAR. Firstly, a flexible channel motion compensation model based on airborne array tomographic SAR multi-channel interference phase is established. Then, based on the rigid multi-channel data and combined with the ground control points, the accurate rigid baseline length and central incidence angle are obtained through the least square method and the global optimal search algorithm. Finally, the flexible motion error is inverted according to the multi-channel interference phase and, combined with the motion compensation model, the flexible data are compensated in the time domain. The details of this process are presented below:

1. The rigid channel is imaged using traditional methods and calibrated by the method introduced in Section 2.2 in combination with the information from calibration points to obtain the central incidence angle under the scene;
2. The flexible channel combines the distributed POS data for 2D imaging to obtain the tracking data before operation and compensation;
3. Following the principle of flexible motion error estimation introduced in Section 2.3, the flexible motion error is estimated by combining the interferogram;
4. According to the motion compensation principle introduced in Section 2.1, the flexible motion error is added to the original data before motion compensation;
5. Two-dimensional imaging and interference processing are reperformed;
6. Steps 2 to 6 are repeated until the coherence coefficient of the interferogram is greater than 0.9;
7. Two-dimensional images with good a focusing effect, and multi-channel interferograms with improved interference performance, are obtained;
8. The 3D result map of multichannel reconstruction is obtained through multi-channel registration, amplitude and phase correction, sparse reconstruction, and other steps.

The iterative solution to the array flexible SAR motion error is presented in Algorithm 1.

Algorithm 1 Iterative solution to array flexible SAR motion error.

```

Input: Flexible channel data  $s_1$  and rigid channel data  $s_2$ .
Initialization: Interference results  $s_3 = s_1 \cdot * s_2, s_3$ 
Step 1: Set  $3 \times 3$  sliding window. Use the sliding window to obtain the interferogram result  $s_3$ ;
Step 2: Calculate according to the coherence coefficient calculation formula  $r = \frac{|data_3|}{\sqrt{data_1^2 * data_2^2}}$ 
while the coherence coefficient  $r > 0.9$ ;
Step 3: Calculate the interference phase  $\delta\phi$  and the correlation coefficient  $r_1$  of data3;
Step 4: The maximum row  $m$  of the average value of the recorded azimuth correlation coefficient is the starting point ;
Step 5: Calculate the maximum deviation of the correlation coefficient  $\delta\phi$  between each azimuth and row  $m$  ;
Step 6: Calculate the distance to  $\phi$  points corresponding to one wavelength;
Step 7: Calculate the offset according to Section 2.3;
Step 8: Calculate the deviation in distance and elevation directions in combination with the lower view angle calculated in Section 2.2;
Step 9: Add the deviation back to the data before operation and compensation, and re-image;
Step 10: Calculate the correlation coefficient  $r$ .
end
Output: Output the current compensation data  $s_e$ .
```

The global optimization, combined with least squares for the flexible baseline, is presented in Algorithm 2.

Algorithm 2 Global optimization combined with least squares for the flexible baseline.

Input: Flexible channel data s_1 and rigid channel data s_2 , POS information y_{ref} and z_{ref} , point target information height h , and geodetic coordinate y

. **Initialization:** Interference results $s_3 = s_1 * s_2$, s_3 and phase unwrapping results $\Delta\phi$.

Construct initial solution

Step 1: Calculate $B = \sqrt{(y_{ref}(1,n) - y_{ref}(1))^2 + (z_{ref}(1,n) - z_{ref}(1))^2}$

Calculate $\theta = a \tan(y/(H-h))$

Let $A = zeros(size(y,2),3)$

$A(:,1) = \sin\theta$

$A(:,2) = -\cos\theta$

$A(:,3) = \frac{\lambda}{4\pi*ones(size(y,2),1)}$

Step 2: Find the least squares solution $B = \frac{A'*A}{(A'*(\frac{\lambda*\Delta\phi'}{4\pi}))}$

Calculate global optimal solution

Step 3: Calculate $\alpha = atan\left(\frac{z_{ref}(1,n)-z_{ref}(1)}{y_{ref}(1,n)-y_{ref}(1)}\right)$

Step 4: Obtain the central incidence angle from the Equation (10);

Step 5: According to result, construct the minimization function from the Equation (9);

Step 6: Perform global search until function $F = 0$.

Output: Output α , B and ϕ .

The flow chart is shown in Figure 4.

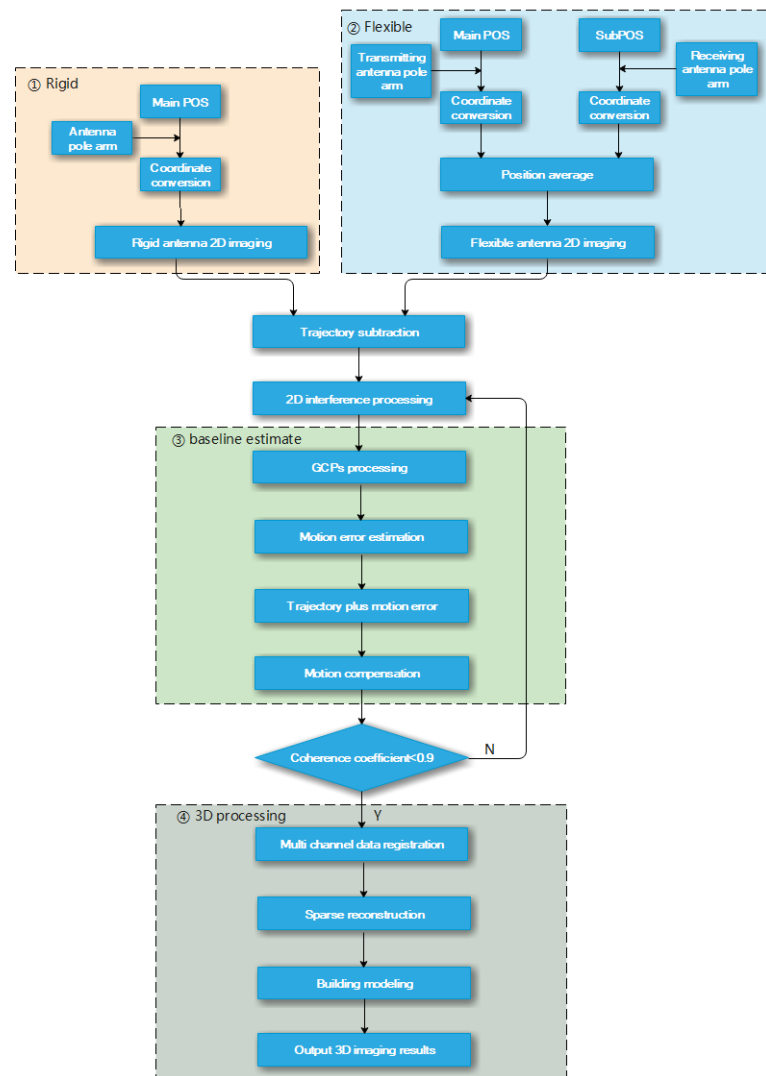


Figure 4. The improved 3D imaging method.

It is worth mentioning the processing of elevation direction in sparse processing. The phase error has a great impact on sparse reconstruction, thus affecting the elevation resolution. Therefore, the proposed method improves the elevation resolution by eliminating the impact of phase error. The procedure of the proposed method is shown above. After running the proposed method, the flexible motion error can be obtained using the principle of flexible motion error estimation, and the error can be added back to the original motion compensation data for accurate imaging. In this way, data support can be provided for subsequent 3D imaging.

4. System

This experiment system adopts the airborne array flexible SAR system developed by AIRCAS. The specific system structure is illustrated in Figure 5. To verify the performance of the flexible baseline, the experimental system simulates the movement of flexible antennae using motor control on a rigid structure.



Figure 5. Schematic diagram of the system.

The key parameters of array tomographic flexible SAR are presented in Table 1. The experimental data were obtained from the flight in Chengdu, Sichuan Province in 2021. The rigid short baseline consisting of belly-mounted antennas was 0.8 m, and the flexible long baseline consisting of wing-mounted antennas was 1.6 m.

Table 1. The parameters of airborne array flexible SAR.

Parameter	Symbol	Value
Flight height	H	5 km
Center Frequency	f_c	15 GHz
Bandwidth	B_w	500 MHz
Rigid baseline length	B_r	0.8 m
Flexible baseline length	B_f	1.6 m
Flight velocity	v	80 m/s
Horizontal inclination of baseline	α	0°

This system was equipped with a distributed POS system to record the carrier attitude in real-time. The left POS system and the right POS system were mounted on the two flexible nodes to measure the flexible antenna attitude in real-time. The main POS system was attached to the rigid node to measure the antenna attitude of the rigid node in real-time. The accuracy is shown in Table 2. During the calculation of motion information, the bias of the accelerometer leads to cumulative errors in the speed and position information calculated by integration. In this paper, the position and speed information provided by satellite navigation were used to correct the cumulative error, and the influence of accelerometer bias on the motion information was reduced.

Table 2. The parameters of distributed POS.

Parameter	Main POS	Sub POS
Height measurement accuracy	5 cm	10 cm
Gyroscopic drift	0.01°/h	0.1°/h
Accelerometer bias	10 µg	20 µg

The baseline jitter frequency was set to 10 r/min, and the height change was within [−2 cm, 2 cm]. A period of time was selected for POS data verification, as shown in the figure below. Figure 6a shows the POS data of five channels before operation and compensation, and Figure 6b shows the flexible channel POS data minus rigid channel POS data. The flexible antenna was 1 and 5, and the rigid antenna was 2, 3, and 4. There are 10 channels in total, of which channel 1, channel 5, channel 6, and channel 10 were flexible channels, and the rest were rigid channels.

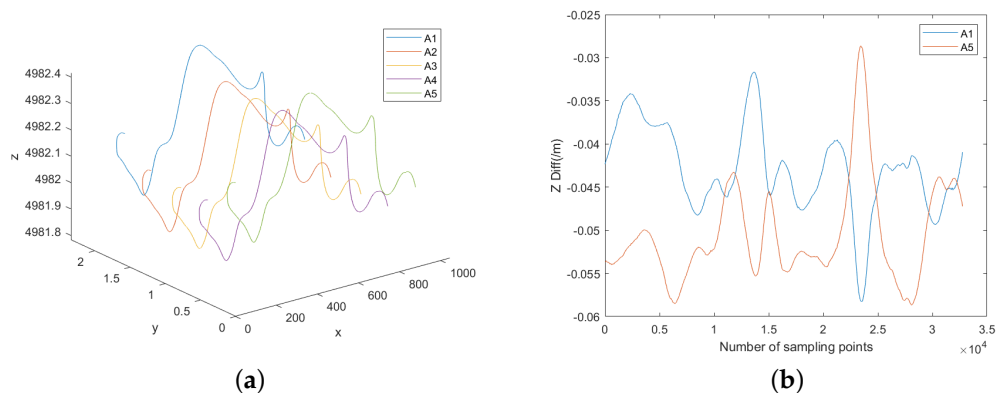


Figure 6. The change in the POS trajectory. (a) The POS trajectory; (b) the jitter trajectory of the flexible antenna.

The jitter frequency and height difference are within a reasonable range, and the data are valid, which supports the verification of the proposed method.

5. Experimental Results and Analysis

Simulation experiments were conducted first, verify the effectiveness of the proposed method. The specific verification step is to add the known error to the rigid POS data of the system, and then apply the proposed method to estimate and compensate. During actual data-processing, the flight test results of the airborne array flexible SAR in Chengdu, Sichuan Province were selected, and the selected scenes included a large range of flat farmland. Specifically, the sub-aperture motion compensation algorithm achieved a higher estimation accuracy, so this paper used the sub-aperture motion compensation algorithm for comparison [18]. During real data experiments, the imaging results of the new transfer alignment algorithm were also compared with the imaging results of a single POS [25].

5.1. Simulation Experiments

In this section, to verify the effectiveness of the proposed method, the simulation data adopted the array flexible SAR data of three rigid channels, namely channel 2, channel 3, and channel 4. As the interference fringe changes along the azimuth, 11,384 points were selected in the azimuth direction, and 5000 points were selected in the distance direction. The synthetic aperture length was $R_{\min} * \theta = 300$ m; the azimuthal point spacing was 0.12 m, which corresponded to the actual scene, with a length of 1366 m, about 4.5 areas of synthetic aperture length; the distance from the azimuthal point spacing was 0.1 m, which corresponded to the actual scene with a length of 500 m. Before the motion compensation

in channel 3, the error shown in Figure 7 was added to the POS data along the vertical and horizontal directions.

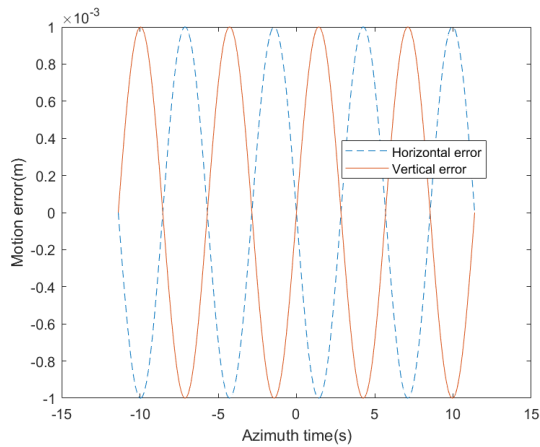


Figure 7. Vertical and horizontal errors.

Then, channel 3 with POS was re-imaged with error data and used to create interference for channel 2 and channel 4. The proposed method was used for error estimation, and the error results of this iterative estimation are presented in Figure 8.

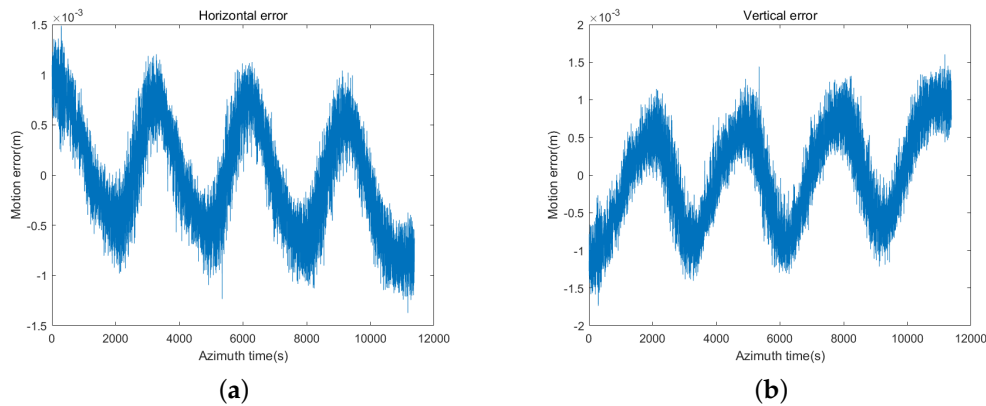


Figure 8. Estimation error. (a) Horizontal error; (b) vertical error.

The motion compensation method proposed in this paper was compared with the sub-aperture motion compensation method. The reconstructed interference fringes and coherence coefficients of channel 3 and channel 4 are shown in Figure 9.

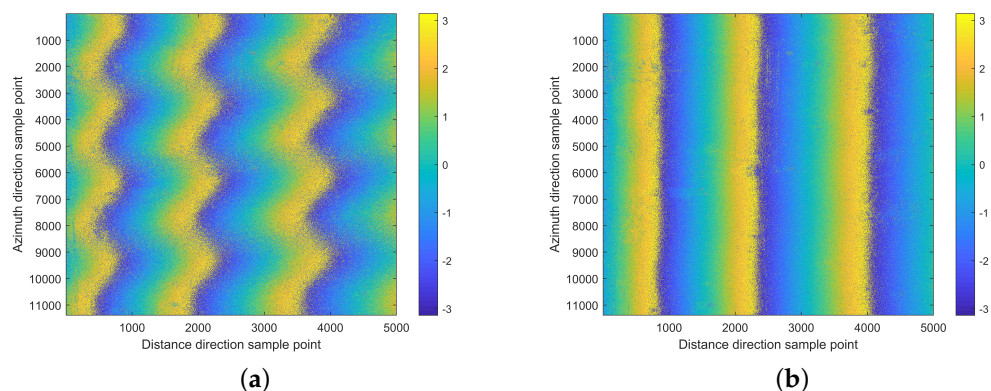


Figure 9. The comparison of interference fringe results. (a) The comparison method; (b) the proposed method.

Figure 9 shows that the interference fringes processed with the sub-aperture compensation method are still curved, and the interference fringes processed with the proposed method are linear. The coherence coefficient graph and the coherence coefficient statistical histogram are illustrated in Figure 10.

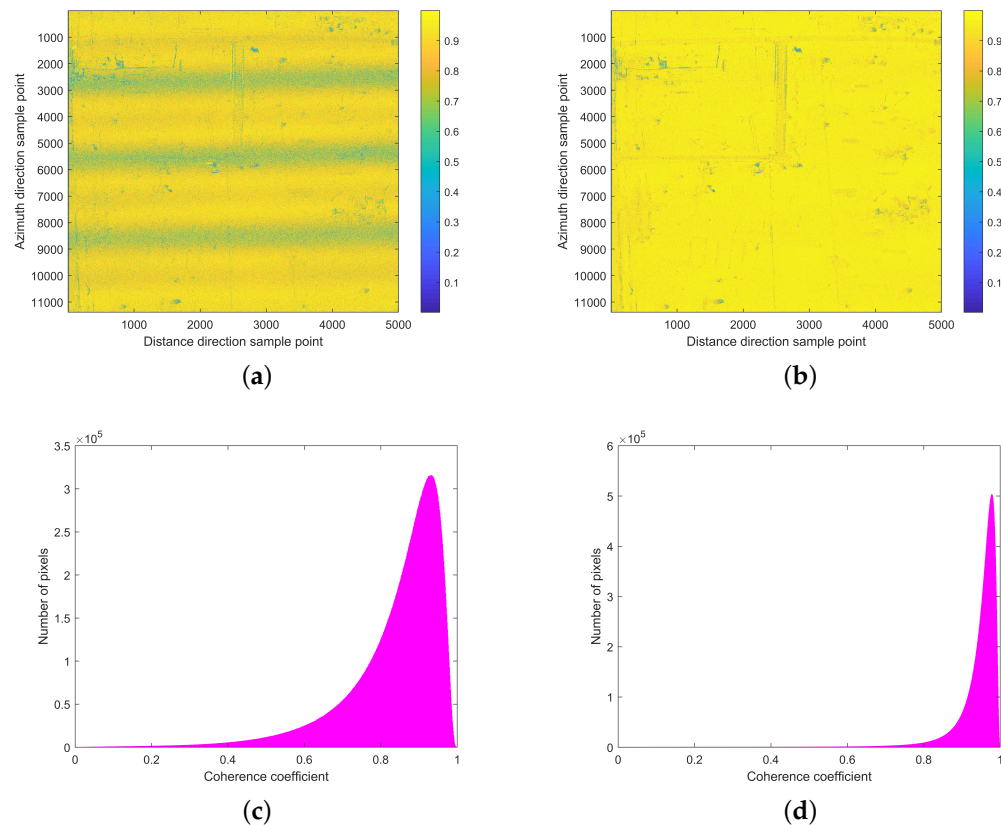


Figure 10. The comparison results. (a) The comparison method’s coherence coefficient diagram; (b) the proposed method’s coherence coefficient diagram; (c) the comparison method’s coherence coefficient statistical histogram; (d) the proposed method’s coherence coefficient statistical histogram.

Figure 10a,c shows that, compared with the traditional imaging method, the comparison method improves sub-aperture compensation. However, there is still residual motion error, and the coherence coefficient is about 0.8. In Figure 10b,d, the proposed method is used for estimation and compensation. The estimation and compensation results are more accurate, and the coherence coefficient can reach 0.95.

Using the above operation and compensation results for imaging, the interference fringes of channel 2 and channel 3 are presented in Figure 11.

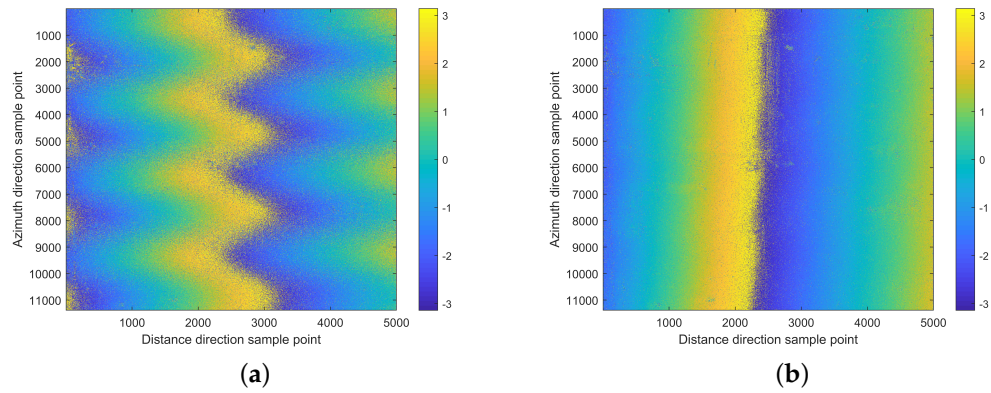


Figure 11. The comparison of interference fringe results. (a) The comparison method; (b) the proposed method.

Figure 11 shows that the interference fringes processed by the sub-aperture compensation method are still curved, and the interference fringes processed by the proposed method are linear. Additionally, the coherence coefficient graph and the coherence coefficient statistical histogram of the two methods are illustrated in Figure 12.

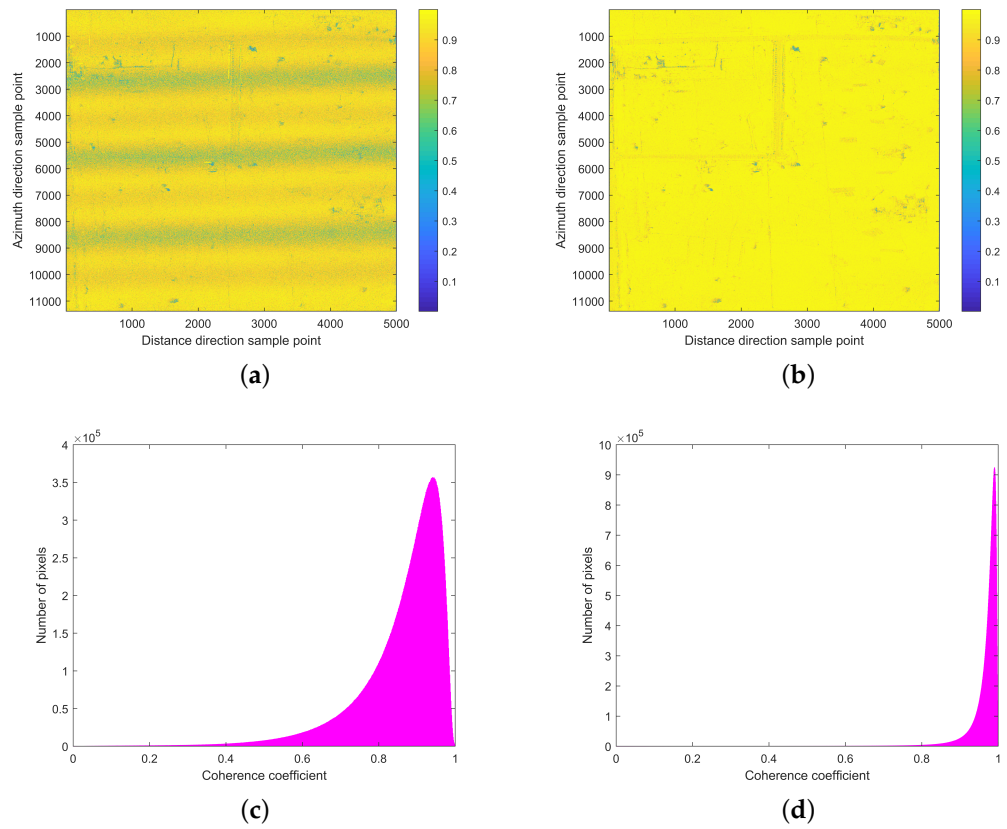


Figure 12. The comparison results. (a) The comparison method coherence coefficient diagram; (b) the proposed method coherence coefficient diagram; (c) the comparison method coherence coefficient statistical histogram; (d) the proposed method coherence coefficient statistical histogram.

Next, the imaging performance of the point targets was compared. The 2D results are shown in Figure 13.

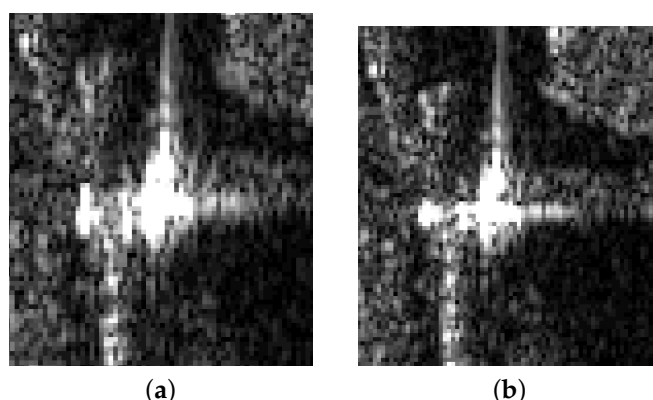


Figure 13. The comparison of 2D results of point targets. (a) The comparison method; (b) the proposed method.

The results of qualitative analysis indicators are presented in Table 3. The results of range and azimuth direction, resolution, integral sidelobe ratio (ISLR), and peak sidelobe ratio (PSLR) are analyzed.

The simulation data confirm the effectiveness of the proposed method, and then the actual data processing was conducted.

Table 3. Point target comparison results of different methods.

Method	Range			Azimuth		
	Resolution (m)	PSLR (dB)	ISLR (dB)	Resolution (m)	PSLR (dB)	ISLR (dB)
method 1 ¹	0.13	−8.15	−10.02	0.17	−22.74	−6.01
method 2 ²	0.13	−8.26	−10.67	0.17	−22.49	−10.23

¹ This is the comparison method [18]. ² This is the proposed method.

5.2. Real Data Experiments

In this section, to verify the effectiveness of the proposed method, flight test data of airborne array flexible SAR in Chengdu, Sichuan Province, were selected. The scene was distributed with multiple calibration points along the distance direction, and located in a flat area.

The system has ten channels, including four flexible channels and six rigid channels. The flexible channel has two channels at the outermost side and a rigid channel at the inner side. Since $2N_t > 3N_p$, N_t and N_p are the number of channels and the number of overlapping layers, the reconstruction requirements of multiple overlapping layers in urban areas was satisfied, and 3D reconstruction could be realized. Meanwhile, as distributed POS imaging is involved, the flexible channel data could be aligned with the azimuth data by applying the method proposed in [32]. After alignment, the flexible channel was imaged using the method described in Section 3, and then aligned with the flexible channel data along the azimuth, in combination with the rigid multi-channel data. The rigid channel 2D imaging method was consistent with the original imaging method, and should be consistent with the method proposed in [18] for the flexible channel.

The principle of scene selection is to locate the calibration point in the central area, from the first time the transmitting beam shines on the calibration point at the far end of the azimuth to the last time it shines on the calibration point at the nearest end of the azimuth. Since the length of the synthetic aperture is 300 m, 32,768 pulses were selected to connect the calibration point area, with 14,000 points in the distance direction, and the calibration point was located in the central area. The scene selection result is shown in Figure 14.



Figure 14. Processing building 2D SAR imaging.

After obtaining the central incidence angle through the calibration method introduced in Section 2, the flat area behind the image was selected to verify the proposed method, and re-imaging was performed according to the selected range. The advantages of the proposed method are illustrated by comparison with the single-node POS, sub-aperture compensation method [18] and coherence coefficient diagram, coherence coefficient histogram, and interference phase diagram of channel 1 and channel 3, using the proposed method. The results are illustrated in Figure 15.

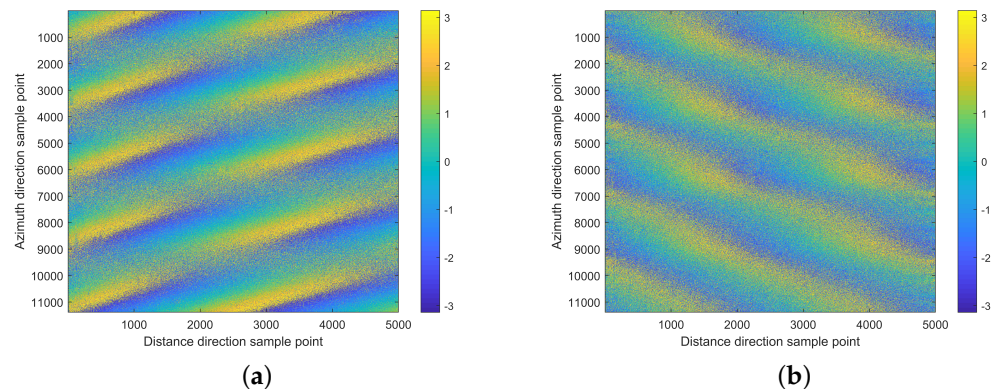


Figure 15. The comparison of interference fringe results. (a) The main POS imaging; (b) the left POS imaging.

Figure 15 shows that the stripes in the single POS processing result are wrong. The coherence coefficient diagram and the coherence coefficient statistical histogram are presented in Figure 16.

Figure 16a,c shows that there is a low-coherence area in the coherence coefficient diagram of the single POS imaging method of the master node, and the average coherence coefficient is about 0.68. Figure 16b,d shows that the coherence coefficient of the POS imaging method using the right node is poor, and the coherence coefficient is only 0.57. Then, the document fusion method was adopted, and the estimation and compensation performance were compared after using the fusion method [32]. The comparison of interference fringe results of channel 1 and channel 3 is shown in Figure 17.

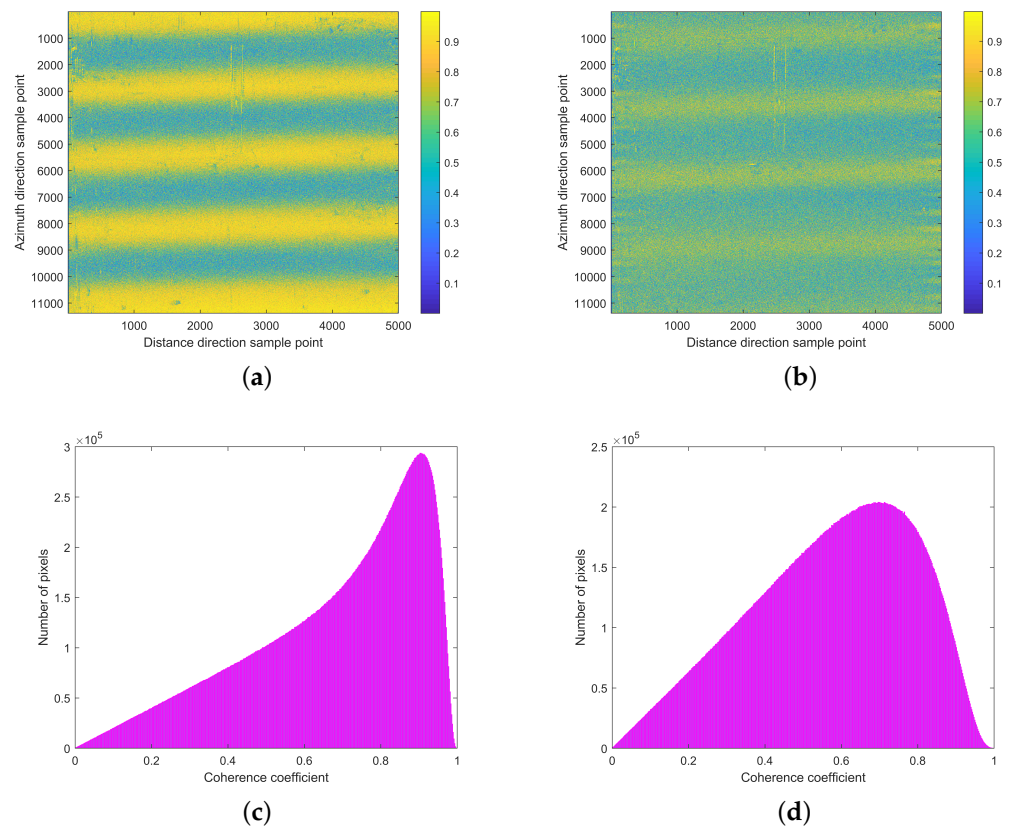


Figure 16. The comparison results. (a) The main POS imaging coherence coefficient diagram; (b) the left POS imaging coherence coefficient diagram; (c) the main POS imaging coherence coefficient statistical histogram; (d) the left POS imaging coherence coefficient statistical histogram.

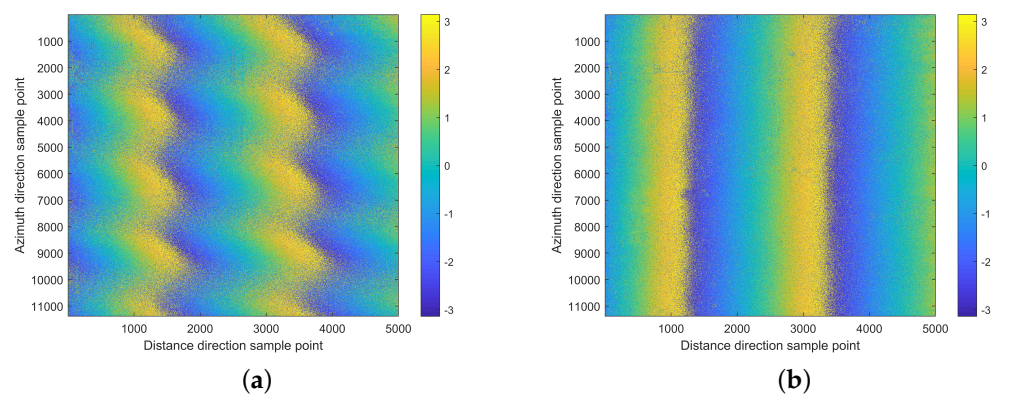


Figure 17. The comparison of interference fringe results. (a) The comparison method; (b) the proposed method.

Figure 17 indicates that the interference fringes processed with the sub-aperture compensation method are still curved, and the interference fringes processed with the proposed method are linear. The coherence coefficient diagram and the coherence coefficient statistical histogram are illustrated in Figure 18.

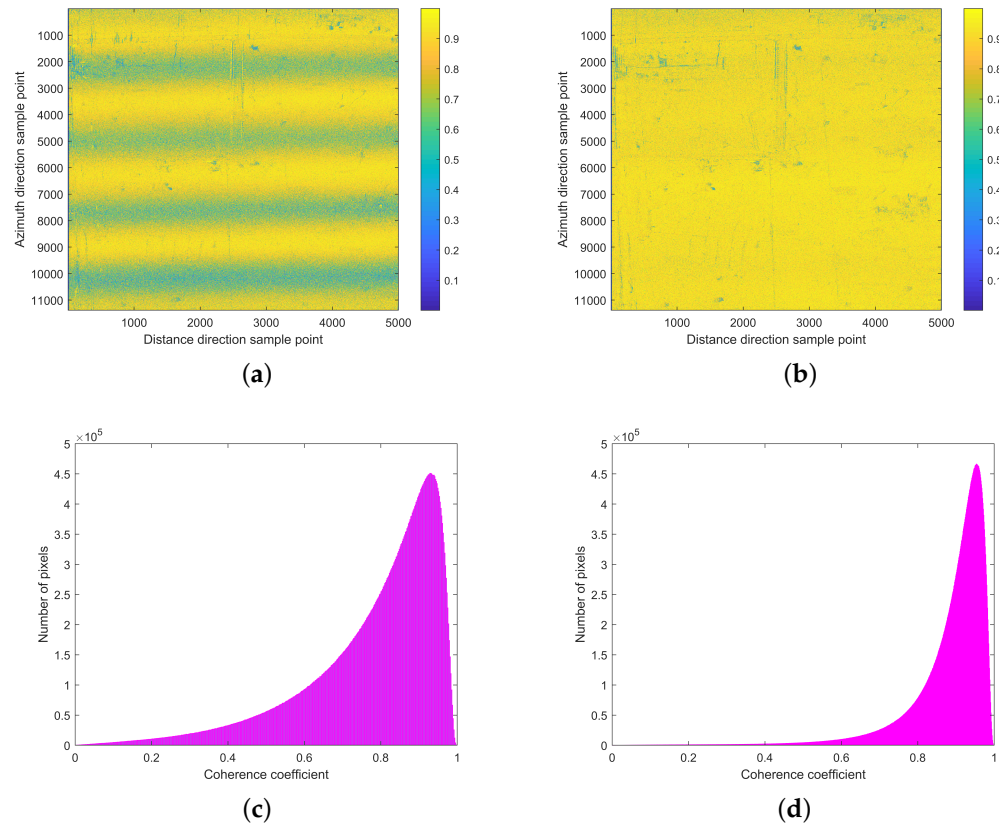


Figure 18. The comparison results. (a) The comparison method coherence coefficient diagram; (b) the proposed method coherence coefficient diagram; (c) the comparison method coherence coefficient statistical histogram; (d) the proposed method coherence coefficient statistical histogram.

Figure 18a,c shows that the comparison method improves sub-aperture compensation compared with traditional imaging methods, but there is still residual motion error, and the average coherence coefficient is about 0.78. Figure 18b,d shows that the estimation and compensation results are more accurate, and the coherence coefficient can reach 0.89.

Then, the above operation compensation results were used for imaging, and a comparison of interference fringe results of channel 1 and channel 2 is presented in Figure 19.

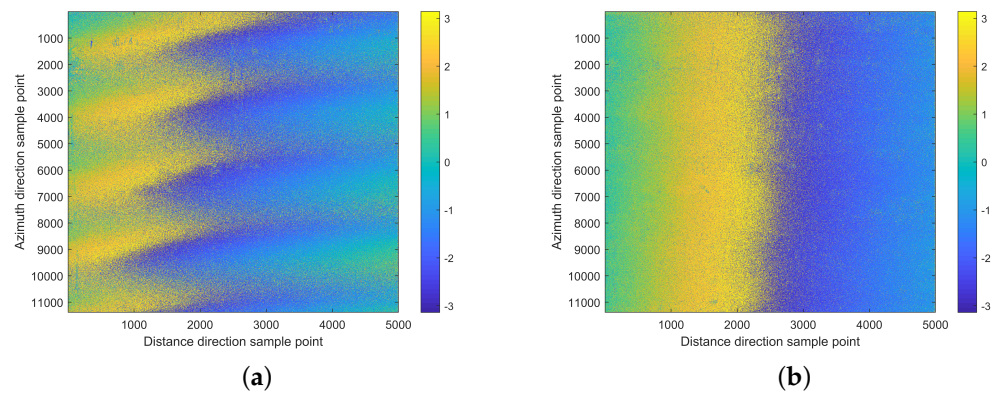


Figure 19. The comparison of interference fringe results. (a) The main POS imaging; (b) The left POS imaging.

Figure 19a shows that the interference fringes processed by the sub-aperture compensation method are still curved. Figure 19b shows that the interference fringes processed

using the proposed method are linear. The coherence coefficient diagram and the coherence coefficient statistical histogram are shown in Figure 20.

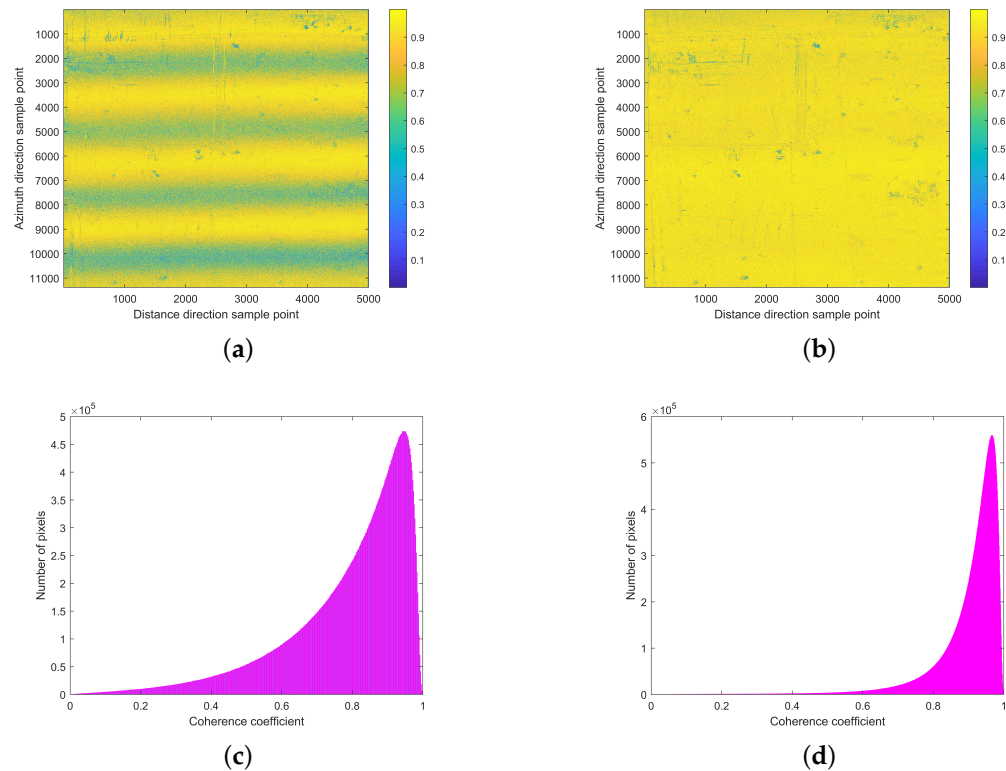


Figure 20. The comparison results. (a) The comparison method coherence coefficient diagram; (b) the proposed method coherence coefficient diagram; (c) the comparison method coherence coefficient statistical histogram; (d) the proposed method coherence coefficient statistical histogram.

Meanwhile, the mean values of the coherence coefficient of the four methods were calculated, as shown in Figure 21.

Then, the imaging performance of point targets was compared. The 2D results are shown in Figure 22.

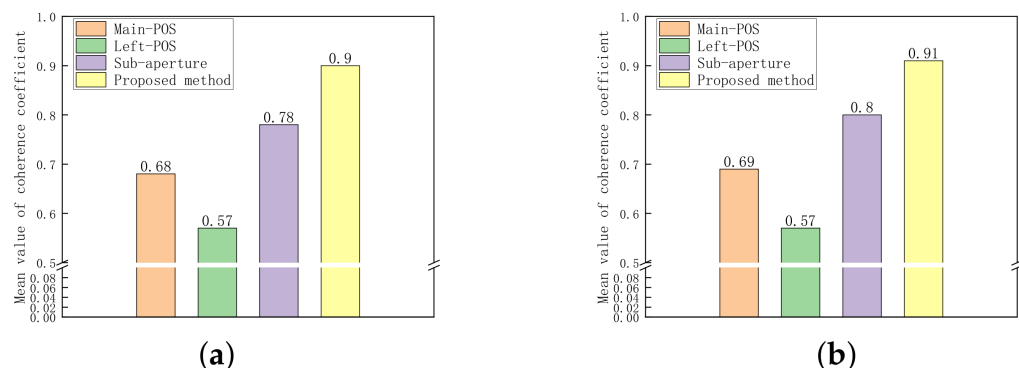


Figure 21. The mean values of coherence coefficient. (a) channel 1 and channel 3; (b) channel 1 and channel 2.

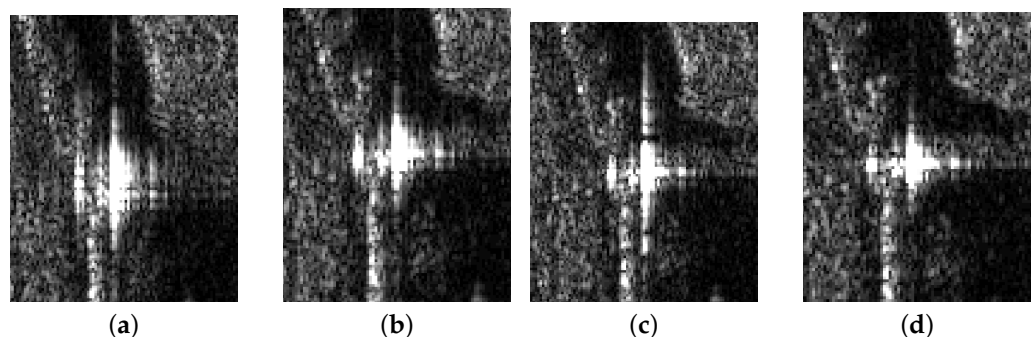


Figure 22. The comparison of 2D results of point targets. (a) The main POS imaging; (b) the left POS imaging; (c) the comparison method; (d) the proposed method.

The results of qualitative analysis indicators are presented in Table 4. The results of range and azimuth direction, resolution, ISLR, and PSLR were analyzed.

Table 4. Point target comparison results of different methods.

Method	Range			Azimuth		
	Resolution (m)	PSLR (dB)	ISLR (dB)	Resolution (m)	PSLR (dB)	ISLR (dB)
method 1 ¹	0.13	−8.73	−10.14	0.17	−7.59	−4.48
method 2 ²	0.13	−8.98	−10.17	0.17	−3.61	−1.89
method 3 ³	0.13	−8.71	−10.12	0.17	−10.21	−6.06
method 4 ⁴	0.13	−8.93	−10.13	0.17	−13.45	−8.09

¹ This is the main POS imaging method [25]. ² This is the right POS imaging method [25]. ³ This is the comparison method [18]. ⁴ This is the proposed method.

Next, the point cloud results of the last two processing methods were compared, and the comparison results are shown in Figure 23.

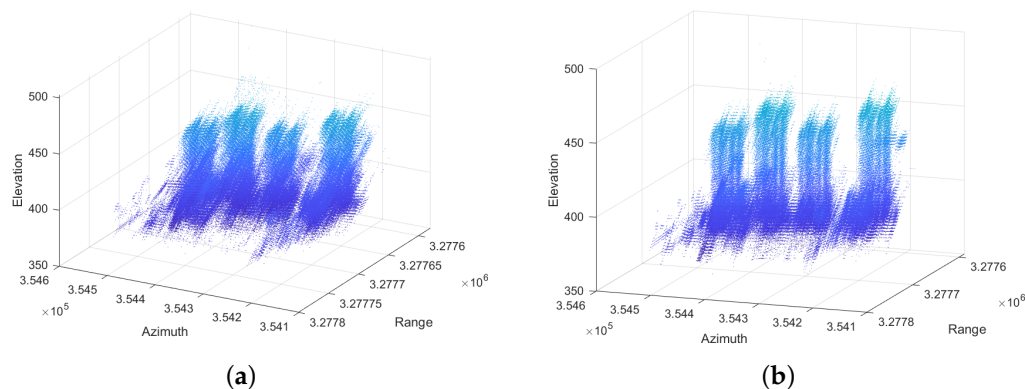


Figure 23. The comparison of 3D reconstruction point cloud results. (a) The comparison method; (b) the proposed method.

Finally, the 3D results of large-area reconstruction using the proposed method are illustrated in Figure 24.

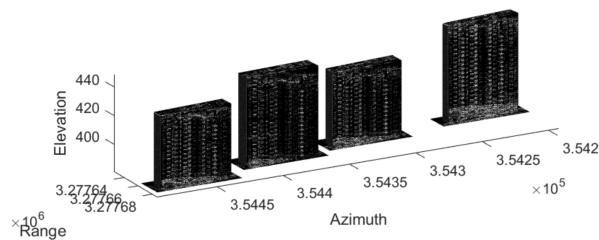


Figure 24. 3D reconstruction results.

6. Discussion

The comparison of simulation results in Figure 9 indicates that the proposed method is more effective than the sub-aperture estimation method. Figure 9a,b shows the 2D interference results of the two methods on rigid channel 3 and channel 4, respectively. The comparison method [18] still has a residual motion error, which is reflected in the bending of the interference fringes along the azimuth, but the proposed method does not suffer from this problem. Figure 10a,b shows that there is a low-coherence region in the coherence coefficient results of the comparison method, while the results of the proposed method do not contain this region. Figure 10c,d shows that the coherence coefficient histogram of the comparison method is about 0.85, while that of the proposed method is mainly about 0.95 and more concentrated. Figures 11 and 12 present the 2D interference results of rigid channels channel 2 and channel 3, which are consistent with those in Figures 9 and 10. By comparing the performance of point targets, it can be seen from the figure that the range resolution and other indicators of the 2D imaging results obtained using this method remain unchanged, but there is a great improvement in the azimuth, especially ISLR. These results demonstrate the advantages of the proposed method.

Meanwhile, the actual data are compared. Figure 15 presents a comparison result [25] obtained using a single POS imaging. The interference phase diagram in Figure 15a,b indicates that there are low-coherence regions, and the imaging results of the master node are better than those of the sub-nodes. This is because the imaging tracks of other rigid channels are calculated by the master node through the lever arm, so that they are consistent. When the imaging results of the right node interfere with the imaging results of the master node, due to the yaw angle, area correspondence and other problems, the resulting coherence coefficient diagram is not as good as that of the main node. According to Figure 16a,b, the coherence coefficient is not high, and according to Figure 16c,d, the interference fringes are not correct. Therefore, the imaging method is subsequently improved [32], and the method proposed in this paper is combined for processing and comparison.

Firstly, the point target performance is compared. The figure shows that the range resolution and other indicators of the 2D imaging results obtained using this method remain unchanged, but there is a great improvement in the azimuth, especially ISLR. Figure 17a,b shows the 2D interference results of the two methods for the flexible channel and rigid channels 1 and 3, respectively, and the comparison method [18] still contains a residual motion error, which is reflected in the bending of interference fringes along the azimuth. However, the proposed method does not contain this region. Figure 18a,b shows a low-coherence region in the coherence coefficient results of the comparison method; the proposed method does not suffer from this problem. Figure 18c,e shows that the coherence coefficient of the comparison method is generally about 0.83, while that of the proposed method is generally about 0.93 and more concentrated. Additionally, Figures 19 and 20 show the 2D interference results of flexible channel 1 and rigid channel 2, which are consistent with those in Figures 17 and 18. Moreover, the statistical diagram of the mean value of the coherence coefficient is shown in Figure 21. The above results reflect the advantages of the proposed method.

As shown in Figure 22, the point cloud reconstruction results of the comparison method in Figure 22a contain many miscellaneous points, and the point cloud reconstruction result is poor. However, after using the proposed method, the point cloud reconstruction result in

Figure 22b is more clear and distinguishable, and there are fewer miscellaneous points, which also reflects the advantages of the proposed method.

7. Conclusions

Airborne array SAR plays an important role in SAR three-dimensional applications such as resource exploration, topographic mapping, and emergency relief. In the airborne array tomographic SAR 3D imaging technology, the baseline length is the main factor that restricts the resolution. An airborne array flexible SAR can increase the baseline length to improve the interference performance by mounting antennae on the wing. However, the existing studies lack results regarding flexible actual data processing and specific motion compensation methods. In this study, a motion error estimation and compensation method for flexible channels is proposed, based on multichannel interferograms of airborne array flexible SAR. Firstly, a flexible channel motion compensation model is established based on the rigid channel interferogram of airborne array tomographic SAR. Then, based on rigid multi-channel data and combined with the ground control points, the accurate rigid baseline length and central incidence angle are obtained using the least square method and the global optimal search algorithm. Finally, the flexible motion error is inversed according to the rigid channel interferogram and, combined with the motion compensation model, the flexible data are compensated in the time domain. The actual data results indicate that, compared with traditional motion error estimation and compensation methods, the proposed method can obtain accurate flexible compensation data and improve the coherence coefficient of airborne array flexible SAR multi-channel data from 0.68 to 0.89. The study results lay a solid foundation for the high-precision mapping of airborne array flexible SAR.

Author Contributions: Conceptualization, L.Y., F.Z. and L.C.; data curation, F.Z. and Y.S.; formal analysis, F.Z. and Y.S.; funding acquisition, F.Z. and L.C.; methodology, L.Y.; project administration, F.Z. and L.C.; resources, Y.S. and Z.L.; validation, L.Y., F.Z. and Z.L.; software, L.Y., F.Z. and D.W.; writing—original draft preparation, L.Y.; writing—review and editing, L.Y., Z.L. and D.W. All authors have read and agreed to the published version of the manuscript.

Funding: This work was supported by the National Key R&D Program of China, No. 2021YFA0715404.

Data Availability Statement: Not applicable.

Acknowledgments: The authors thank all colleagues who participated in the airborne array flexible SAR system design and the acquisition of measured data. The authors would also like to express their gratitude to the anonymous reviewers and the editor for their constructive comments on the paper.

Conflicts of Interest: The authors declare no conflict of interest.

Abbreviations

The following abbreviations are used in this manuscript:

SAR	Synthetic Aperture Radar
3D	Three-dimensional
DEM	Digital Elevation Model
ARTINO	Airborne Radar for Three-dimensional Imaging and Nadir Observation
SRTM	Shuttle Radar Topography Mission
AIRCAS	Aerospace Information Research Institute, Chinese Academy of Sciences
POS	Position and orientation system
LFM	Linear frequency modulation
2D	Two-dimensional
ISLR	integral sidelobe ratio
PSLR	peak sidelobe ratio

References

- Li, X.; Zhang, F.; Li, Y.; Guo, Q.; Wan, Y.; Bu, X.; Liu, Y.; Liang, X. An Elevation Ambiguity Resolution Method Based on Segmentation and Reorganization of TomoSAR Point Cloud in 3D Mountain Reconstruction. *Remote Sens.* **2021**, *13*, 5118. [[CrossRef](#)]
- Chai, H.; Lv, X.; Xiao, P. Deformation Monitoring Using Ground-Based Differential SAR Tomography. *IEEE Geosci. Remote Sens. Lett.* **2020**, *17*, 993–997. [[CrossRef](#)]
- Ho Tong Minh, D.; Hanssen, R.; Rocca, F. Radar Interferometry: 20 Years of Development in Time Series Techniques and Future Perspectives. *Remote Sens.* **2020**, *12*, 1364. [[CrossRef](#)]
- Cazcarra-Bes, V.; Tello-Alonso, M.; Fischer, R.; Heym, M.; Papathanassiou, K. Monitoring of Forest Structure Dynamics by Means of L-Band SAR Tomography. *Remote Sens.* **2017**, *9*, 1229. [[CrossRef](#)]
- Banda, F.; Dall, J.; Tebaldini, S. Single and Multipolarimetric P-Band SAR Tomography of Subsurface Ice Structure. *IEEE Trans. Geosci. Remote Sens.* **2016**, *54*, 2832–2845. [[CrossRef](#)]
- Tebaldini, S.; Nagler, T.; Rott, H.; Heilig, A. Imaging the Internal Structure of an Alpine Glacier via L-Band Airborne SAR Tomography. *IEEE Trans. Geosci. Remote Sens.* **2016**, *54*, 7197–7209. [[CrossRef](#)]
- Frey, O.; Meier, E. 3-D Time-Domain SAR Imaging of a Forest Using Airborne Multibaseline Data at L- and P-Bands. *IEEE Trans. Geosci. Remote Sens.* **2011**, *49*, 3660–3664. [[CrossRef](#)]
- Luo, H.; Li, Z.; Dong, Z.; Yu, A.; Zhu, X. Super-Resolved Multiple Scatterers Detection in SAR Tomography Based on Compressive Sensing Generalized Likelihood Ratio Test (CS-GLRT). *Remote Sens.* **2019**, *11*, 1930. [[CrossRef](#)]
- Zhu, X.X.; Bamler, R. Tomographic SAR Inversion by L_1 -Norm Regularization—The Compressive Sensing Approach. *IEEE Trans. Geosci. Remote Sens.* **2010**, *48*, 3839–3846. [[CrossRef](#)]
- Aghababaee, H.; Ferraioli, G.; Schirinzi, G.; Pascazio, V. Regularization of SAR Tomography for 3-D Height Reconstruction in Urban Areas. *IEEE J. Sel. Top. Appl. Earth Obs. Remote Sens.* **2019**, *12*, 648–659. [[CrossRef](#)]
- Klare, J.; Weiss, M.; Peters, O.; Brenner, A.; Ender, J. ARTINO: A New High Resolution 3D Imaging Radar System on an Autonomous Airborne Platform. In Proceedings of the 2006 IEEE International Symposium on Geoscience and Remote Sensing, Denver, CO, USA, 31 July–4 August 2006; pp. 3842–3845.
- Jordan, R.L.; Caro, E.R.; Kim, Y.; Kobrick, M.; Werner, M.U. Shuttle radar topography mapper (SRTM). In Proceedings of the Microwave Sensing and Synthetic Aperture Radar, Taormina, Italy, 23–27 September 1996; pp. 412–422.
- Fornaro, G. Trajectory deviations in airborne SAR: Analysis and compensation. *IEEE Trans. Aerosp. Electron. Syst.* **1999**, *35*, 997–1009. [[CrossRef](#)]
- Weiß, M.; Ender, J.H.G. A 3D imaging radar for small unmanned airplanes-ARTINO. In Proceedings of the European Radar Conference (EURAD 2005), Paris, France, 3–4 October 2005; pp. 209–212.
- Klare, J.; Cerutti-Maori, D.; Brenner, A.; Ender, J. Image quality analysis of the vibrating sparse MIMO antenna array of the airborne 3D imaging radar ARTINO. In Proceedings of the 2007 IEEE International Geoscience and Remote Sensing Symposium, Barcelona, Spain, 23–28 July 2007; pp. 5310–5314.
- Reigber, A.; Prats, P.; Mallorqui, J. Refined estimation of time-varying baseline errors in airborne SAR interferometry. *IEEE Geosci. Remote Sens. Lett.* **2006**, *3*, 145–149. [[CrossRef](#)]
- Wang, H.; Fu, H.; Zhu, J.; Feng, G.; Yang, Z.; Wang, C.; Hu, J.; Yu, Y. Correction of Time-Varying Baseline Errors Based on Multibaseline Airborne Interferometric Data Without High-Precision DEMs. *IEEE Trans. Geosci. Remote Sens.* **2021**, *59*, 9307–9318. [[CrossRef](#)]
- You, D.; Sun, G.C.; Xia, X.G.; Xing, M.; Li, Y.; Li, B.; Bao, Z. Time-Varying Baseline Error Estimation and Compensation in UAV SAR Interferometry Based on Time-Domain Subaperture of Raw Radar Data. *IEEE Sens. J.* **2020**, *20*, 12203–12216. [[CrossRef](#)]
- Wang, H.; Zhu, J.; Fu, H.; Feng, G.; Wang, C. Modeling and Robust Estimation for the Residual Motion Error in Airborne SAR Interferometry. *IEEE Geosci. Remote Sens. Lett.* **2019**, *16*, 65–69. [[CrossRef](#)]
- Cao, N.; Lee, H.; Zaugg, E.; Shrestha, R.; Carter, W.E.; Glennie, C.; Lu, Z.; Yu, H. Estimation of Residual Motion Errors in Airborne SAR Interferometry Based on Time-Domain Backprojection and Multisquint Techniques. *IEEE Trans. Geosci. Remote Sens.* **2018**, *56*, 2397–2407. [[CrossRef](#)]
- Liu, Y.; Wang, B.; Ye, W.; Ning, X.; Gu, B. Global Estimation Method Based on Spatial-Temporal Kalman Filter for DPOS. *IEEE Sens. J.* **2021**, *21*, 3748–3756. [[CrossRef](#)]
- Franceschetti, G.; Iodice, A.; Maddaluno, S.; Riccio, D. Effect of antenna mast motion on X-SAR/SRTM performance. *IEEE Trans. Geosci. Remote Sens.* **2000**, *38*, 2361–2372. [[CrossRef](#)]
- Wang, B.; Xiang, M.; Chen, L. Motion compensation on baseline oscillations for distributed array SAR by combining interferograms and inertial measurement. *IET Radar Sonar Navig.* **2017**, *11*, 1285–1291. [[CrossRef](#)]
- Gu, B.; Li, J.; Fang, J.; Yuan, X. Airborne Distributed POS Flexible Baseline Measurement Method Based on MCLS. *IEEE Sens. J.* **2019**, *19*, 2087–2095. [[CrossRef](#)]
- Sun, Y.; Gong, X.; Yang, L.; Wang, D.; Zhang, F. A Motion Information Acquisition Algorithm of Multiantenna SAR Installed on Flexible and Discontinuous Structure Based on Distributed POS. *IEEE Trans. Geosci. Remote Sens.* **2022**, *60*, 1–12. [[CrossRef](#)]
- Xiao, L.G.; Jian, X.Z. An innovative transfer alignment method based on federated filter for airborne distributed POS. *Measurement* **2014**, *86*, 165–181.

27. Li, J. and Jia, L. and Gang, L. Multisensor Time Synchronization Error Modeling and Compensation Method for Distributed POS. *IEEE Trans. Instrum. Meas.* **2016**, *11*, 2637–2645.
28. Xiao, L.G.; Ting, T.Q. An innovative distributed filter for airborne distributed position and orientation system. *Aerospace Sci. Technol.* **2021**, *119*, 107155.
29. Aghababaei, H.; Ferraioli, G.; Ferro-Famil, L.; Huang, Y.; Mariotti D'Alessandro, M.; Pascazio, V.; Schirinzi, G.; Tebaldini, S. Forest SAR Tomography: Principles and Applications. *IEEE Geosci. Remote Sens. Mag.* **2020**, *8*, 30–45. [[CrossRef](#)]
30. Xiao, X.Z.; Adam, N.; Brćic, R.; Bamler, R. Space-borne high resolution SAR tomography: Experiments in urban environment using TS-X Data. In Proceedings of the Urban Remote Sensing Event, Shanghai, China, 20–22 May 2009.
31. Ferretti, A.; Prati, C.; Rocca, F. Permanent scatterers in SAR interferometry. *IEEE Trans. Geosci. Remote Sens.* **2001**, *39*, 8–20. [[CrossRef](#)]
32. Ling Yang, Fubo Zhang, M.Q.; Chen, L. 3D Imaging Method of Airborne Array Flexible SAR Based on Distributed POS. *Electron. Lett.* **2022**, *preprint*. [[CrossRef](#)]

Disclaimer/Publisher's Note: The statements, opinions and data contained in all publications are solely those of the individual author(s) and contributor(s) and not of MDPI and/or the editor(s). MDPI and/or the editor(s) disclaim responsibility for any injury to people or property resulting from any ideas, methods, instructions or products referred to in the content.